J. Space Weather Space Clim. 4 (2014) A27
DOI: 10.1051/swsc/2014024

SWSC

REGULAR ARTICLE OPEN ACCESS

Statistics of ionospheric disturbances and their correlation with GNSS positioning errors at high latitudes

Knut Stanley Jacobsen* and Michael Dähnn

Norwegian Mapping Authority, Norway
*Corresponding author: jacokn@kartverket.no

Received 26 May 2014 / Accepted 26 August 2014

ABSTRACT

The Rate Of TEC Index (ROTI) is a commonly used measure of ionospheric activity. ROTI values have been computed every 5 min for the year 2012, for 10 receivers at latitudes from 59° to 79° North. We present the results in geomagnetic coordinates, showing that elevated ROTI values occur mainly in the cusp and nightside auroral oval regions. Elevated ROTI values are more common in the cusp, but in the nightside auroral oval they are stronger.
To investigate the relation to positioning errors, receiver coordinates were computed using the GIPSY software, for the same receivers and time resolution. We found that there is a strong positive correlation between Precise Point Positioning (PPP) error and ROTI for receivers that are affected by space weather. The 3D position error increases exponentially with increasing ROTI. A statistical analysis presents also the risk of having several satellites observing enhanced ROTI values simultaneously, showing that this risk is greater at high latitudes.

Key words. Space weather – Positioning system – Ionosphere (auroral) – Statistics and probability

1. Introduction

Global Navigation Satellite System (GNSS) positioning can suffer from a number of different error sources. During strong ionospheric activity, the ionosphere is the dominant error source for GNSS signals.

The occurrence of scintillation at high latitudes is related to the auroral oval, cusp, and polar-cap patches, through the formation of small-scale plasma structures due to particle precipitation or plasma instabilities (e.g. Weber et al. 1986; Kersley et al. 1995; Aarons 1997; Kivanc & Heelis 1997; Aquino et al. 2005; Krankowski et al. 2006; Skone et al. 2009; Spogli et al. 2009; Burston et al. 2010; Tiwari et al. 2010; Prikryl et al. 2013). It has been observed that phase scintillation occurs more often than amplitude scintillation at high latitudes, and that scintillation is more common on geomagnetically disturbed days in the auroral oval region and close to noon and midnight (Aquino et al. 2005; Spogli et al. 2009; Prikryl et al. 2010; Tiwari et al. 2010; Moen et al. 2013; Prikryl et al. 2013).

The Norwegian Mapping Authority (NMA) operates a national network of GNSS receivers, which is used for positioning services and various studies. In this paper, we investigate the link between PPP errors and the ROTI, which is a commonly used measure of ionospheric activity (see Sect. 2.2). We also investigate the location of the elevated ROTI values in geomagnetic coordinates, and the probability of having multiple satellites affected simultaneously.

The data sources are presented in Section 2. The observations are presented in Section 3 and discussed in Section 4. Finally, Section 5 provides a short summary of our conclusions.

2. Data sources

This study is based on GNSS data from 10 receivers (see Sect. 2.1) for the whole year of 2012. The data has been processed to calculate ROTI (see Sect. 2.2) and PPP coordinates (See Sect. 2.3) at 5 min resolution.

2.1. Receivers

Figure 1 shows the locations of the receivers used in this study, and Table 1 lists their basic information (NYAL and NYA1 are colocated, so only one of them is plotted on the map). All the receivers are owned and operated by NMA. The receivers run with a sample rate of 1 Hz.

2.2. Rate of TEC index (ROTI)

In this study, ionospheric disturbances are measured by the ROTI (Pi et al. 1997). It characterizes small-scale and/or rapid variations of TEC, and is strongly related to scintillation (Basu et al. 1999). Its main advantage over scintillation indices is that it is calculated based on measurements from standard dual-frequency GNSS receivers sampling at 1 Hz, which have been and still are far more common than scintillation receivers.

While the use of dual-frequency observations allows the correction of ionospheric delay to the first order, higher order terms remain. Additional ionospheric error sources include amplitude and phase scintillations, and deviation of signal paths from a straight line due to refraction in the ionosphere. All of these effects may be amplified during periods of increased

Table 1. List of receivers.

ID	Location	Latitude	Longitude	Receiver type	Antenna type
NYAL	Ny-Ålesund	78.93	11.87	Trimble NetRS	AOAD/M_B
NYA1	Ny-Ålesund	78.93	11.87	Trimble NetR8	ASH701073.1
LYRS	Longyearbyen	78.23	15.40	Trimble NetR9	TRM41249.00
HAMC	Hammerfest	70.67	23.66	Trimble NetR5	TRM55971.00
TRO1	Tromsø	69.66	18.94	Trimble NetR8	TRM59800.00
VEGS	Vega	65.67	11.97	Trimble NetR8	TRM59800.00
FOLC	Folling	64.12	11.62	Trimble NetR5	TRM59800.00
HFS4	Hønefoss	60.14	10.24	Trimble NetR5	TRM59800.00
OPEC	Opera	59.91	10.75	Trimble NetR5	TRM55971.00
STAS	Stavanger	59.02	5.60	Trimble NetR8	TRM55971.00

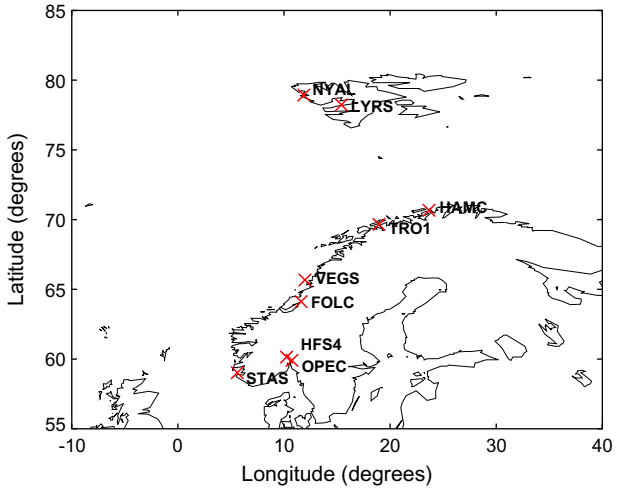

Fig. 1. Geographic locations of the GNSS receivers used in this study.

ionospheric activity, which are generally caused by the interaction between the solar wind and the Earth system. Except for amplitude scintillation, ROTI is expected to be affected by these types of disturbances. ROTI is most closely related to phase scintillations.

The definition of ROTI is given in Section 2.2.1. In this study, the ROTI values are based on 1 Hz measurements ($\Delta t = \frac{1}{60}$ min), and calculated for time intervals of 5 min ($N = 300$). An elevation cutoff of 5° was used. Note that for the results presented in Section 3.3, an elevation cutoff of 30° was applied.

2.2.1. Definition of ROTI

ROTI is defined as the standard deviation of the Rate Of TEC (ROT) over some time interval. It is calculated as follows, where Ln, λ_n, and f_n are the phase measurement, wavelength, and frequency for the nth frequency.

$L_{GF}(i)$ is the geometry-free phase combination at time i

$$L_{GF}(i) = L1(i) \times \lambda_1 - L2(i) \times \lambda_2. \quad (1)$$

ROT (in TECU/minute) is calculated as

$$\mathrm{ROT}(i) = \frac{L_{GF}(i) - L_{GF}(i-1)}{\Delta t \times 10^{16} \times 40.3 \times \left(\frac{1}{f_1^2} - \frac{1}{f_2^2}\right)}. \quad (2)$$

TECU (TEC unit) is defined as 10^{16} electrons per m^2. Δt is the time difference between the epochs, in minutes.

Table 2. Parameters/models used for the GIPSY PPP solution.

GIPSY version	6.1.2
Reference frame	IGS08/IGb08
Elevation angle cutoff	10°
Antenna phase center (receivers)	Absolute based on IGS standard e.g. igs08_1645.atx
Antenna phase center (transmitters)	Absolute based on IGS standard e.g. igs08_1645.atx
Troposphere mapping function	VMF1
Second order ionosphere model	Not applied
Ocean loading	FES2004
Ambiguity resolution	Yes (Bertiger et al. 2010)

Finally, ROTI, calculated over N epochs, is

$$\mathrm{ROTI}(k) = \sqrt{\frac{1}{N}\sum_{j=k-N}^{k}(\mathrm{ROT}(j) - \overline{\mathrm{ROT}})^2}. \quad (3)$$

$\overline{\mathrm{ROT}}$ is the average of ROT for the interval $k\left(\overline{\mathrm{ROT}} = \frac{1}{N}\sum_{j=k-N}^{k}\mathrm{ROT}(j)\right)$.

2.3. Precise point positioning (PPP)

Precise Point Positioning (PPP) is a processing strategy for GNSS observations that enables the efficient computation of high-quality coordinates, utilizing undifferenced dual-frequency code and phase observations by using precise satellite orbit and clock products. More detailed descriptions of PPP can be found in Zumberge et al. (1997) and Kouba & Héroux (2001).

Previous studies by Tiwari et al. (2009) and Moreno et al. (2011) have examined the effects of ionospheric disturbances on PPP calculations at low/equatorial latitudes. Moreno et al. (2011) concluded that the presence of large ROT can induce a significant degradation of the position estimation.

To study how a disturbed ionosphere affects the PPP calculations, we have used the GIPSY software provided by NASAs Jet Propulsion Laboratory (JPL) to compute coordinates for the receivers listed in Table 1. The coordinates were computed with a time resolution of 5 min. Important parameters/models used for the GIPSY PPP solutions are summarized in Table 2.

3. Observations

3.1. ROTI vs. PPP error

To investigate the link between ROTI and PPP positioning errors, we calculated the mean ROTI across all observed

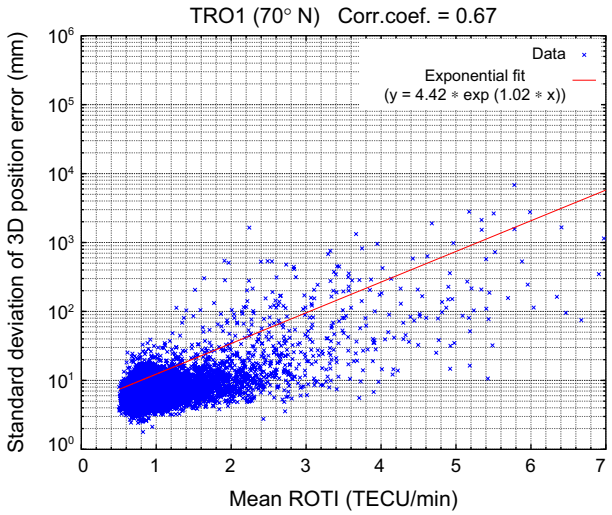

Fig. 2. Scatter plot of mean ROTI vs. 3D position error. The red line shows an exponential fit to the data.

Table 3. Correlation coefficients and fit parameters.

ID	Corr. coeff.	a	b
NYAL	0.46	1.95	1.67
NYA1	0.39	4.54	0.75
LYRS	0.47	13.33	0.99
HAMC	0.66	8.24	0.88
TRO1	0.67	4.42	1.02
VEGS	0.49	5.05	0.90
FOLC	0.41	8.40	0.83
HFS4	0.09	18.99	0.13
OPEC	0.14	7.42	0.24
STAS	0.16	6.05	0.31

satellites for every 5 min, at the times corresponding to the PPP solutions.

The long-term trend was removed from the PPP solutions by subtracting a linear fit to the coordinate time series for the entire year, for each receiver. The 3D position error (P_{3D}) was then defined as the offset of the detrended coordinate from its median value (x_0, y_0, z_0) and calculated for each epoch i as:

$$P_{3D}(i) = \sqrt{(x(i) - x_0)^2 + (y(i) - y_0)^2 + (z(i) - z_0)^2}. \quad (4)$$

Then, for each receiver and each hour we calculated the mean ROTI ($\overline{\mathrm{ROTI}_{1h}}$) and the standard deviation of P_{3D} (σ_{3D_1h}). These hourly resolution values were then correlated, for an exponential relationship:

$$\sigma_{3D\_1h} = a \times e^{(b \times \overline{\mathrm{ROTI}_{1h}})}, \quad (5)$$

where a and b are the parameters of the fit.

Figure 2 shows an example of an exponential fit. A summary of the fitting and correlation results for all the receivers is listed in Table 3.

To further distill the data of the kind shown in Figure 2, we binned the hourly 3D position errors by the hourly ROTI value in intervals of 0.5 TECU/min and computed the mean and standard deviation of the 3D position errors within each bin. The results are presented in Figures 3 and 4. The number of samples in each bin is shown in Figure 5. Note that results are not calculated, and thus not shown in the figures, for bins that contain less than 10 samples. The receivers FOLC, VEGS, TRO1, HAMC, LYRS, and NYA1 have good coverage across the set of bins.

3.2. Low elevation effects on ROTI

The influence of the ionosphere on the GNSS signal is proportional to the length of the signal path through the ionosphere. The length of the signal path depends on the satellite elevation, being greater at lower elevations. To investigate the impact of this, we have binned all the 5 min ROTI values by elevation and then taken the median ROTI within each bin. The bin size is 1°, and the range of elevations is from 5° to 85°. Elevations above 85° are not included because there are few measurements at those elevations. Since most days have negligible ionospheric activity, this results in an elevation distribution of ROTI for calm ionospheric conditions. Other intermittent conditions (e.g. measurement errors, increased noise due to weather effects) are also removed by taking the median, and conditions that do not depend on elevation will contribute equally to all bins. Figure 6 shows the result. It can be seen that the ROTI values are highest at low elevations. From there the values decrease exponentially until 40° elevation. At 40° a level is reached, where the ROTI values do not change significantly for higher elevations. The red line in the plot shows an exponential function of the length of the GNSS signal path (e^L) that the signal has to pass through. The line is scaled to intersect the ROTI (blue line) at 30° elevation. The length of the GNSS signal path (L) is modeled using the standard mapping function:

$$MF(E) = \sqrt{1 - \left(\frac{R_E \times \cos(E)}{R_E + h}\right)^2}, \quad (6)$$

where E is the elevation, R_E is the radius of the Earth, and h is the height of the ionosphere layer (here defined as 350 km). The mapping function (MF) is the ratio between the vertical thickness of the ionosphere and the slant thickness of the ionosphere for the elevation E. The GNSS signal path length is thus the inverse of the mapping function:

$$L(E) = \frac{1}{MF(E)}. \quad (7)$$

Without specifying the thickness of the ionosphere, the GNSS signal path length as specified here does not have a physical unit. This is acceptable, since we are only interested in its shape as a function of elevation. The exponential function matches the observed ROTI at low elevations (<30°), but at higher elevations the ROTI levels off and shows almost no variation with elevation. This indicates that at high (>30°) elevations, the effect caused by the variation of the signal path length through the ionosphere is small compared to other effects that influence the ROTI value.

The results show that to compare ROTI values from low elevation satellites with other ROTI values, with an intention of investigating the condition of the ionosphere, they need to be scaled. Alternatively, one may avoid the issue by excluding data from satellites below 30° elevation. If one is instead studying the effects of ROTI on the receiver itself, the values should not be scaled, as the ROTI value is indeed a measure of the disturbance that the receiver observes in the GNSS observables. This should be taken into account when studying space weather with the use of ROTI.

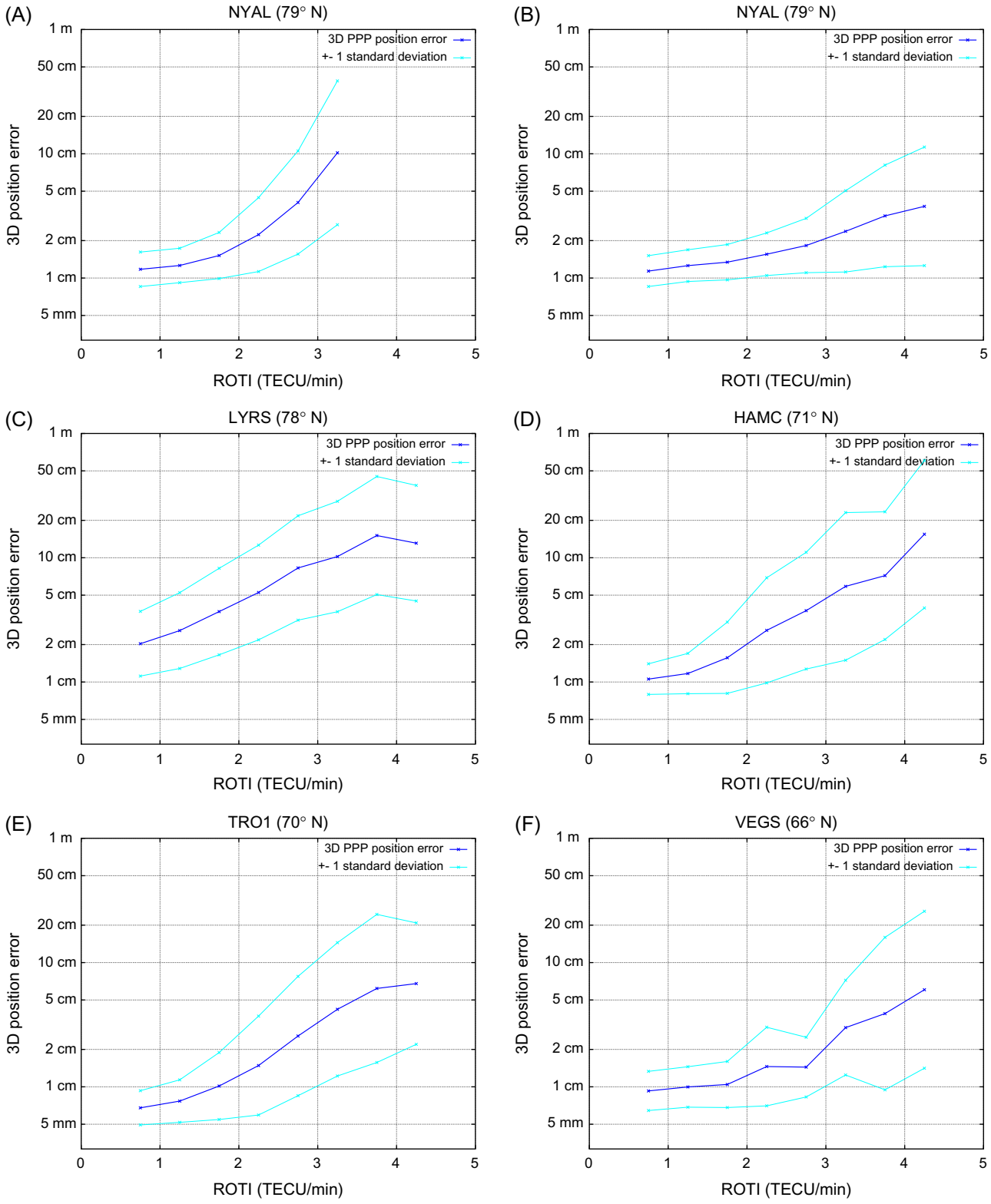

Fig. 3. Statistical relationship between mean ROTI and 3D position error, for these receivers: (A) NYAL, (B) NYA1, (C) LYRS, (D) HAMC, (E) TRO1, (F) VEGS.

3.3. ROTI occurrence statistics

Based on the data shown in Figure 6, we chose an elevation cutoff of 30° for the analysis to avoid the elevation dependency of ROTI values. The ROTI data were binned by magnetic latitude (MLAT) and magnetic local time (MLT), at a resolution of 1° and 1 h. Figure 7 shows the number of samples for each bin. Most bins have between 1000 and 10000 samples, which is a good amount of samples for a statistical analysis. Unfortunately, there is no data coverage at latitudes above 80°. This is due to the

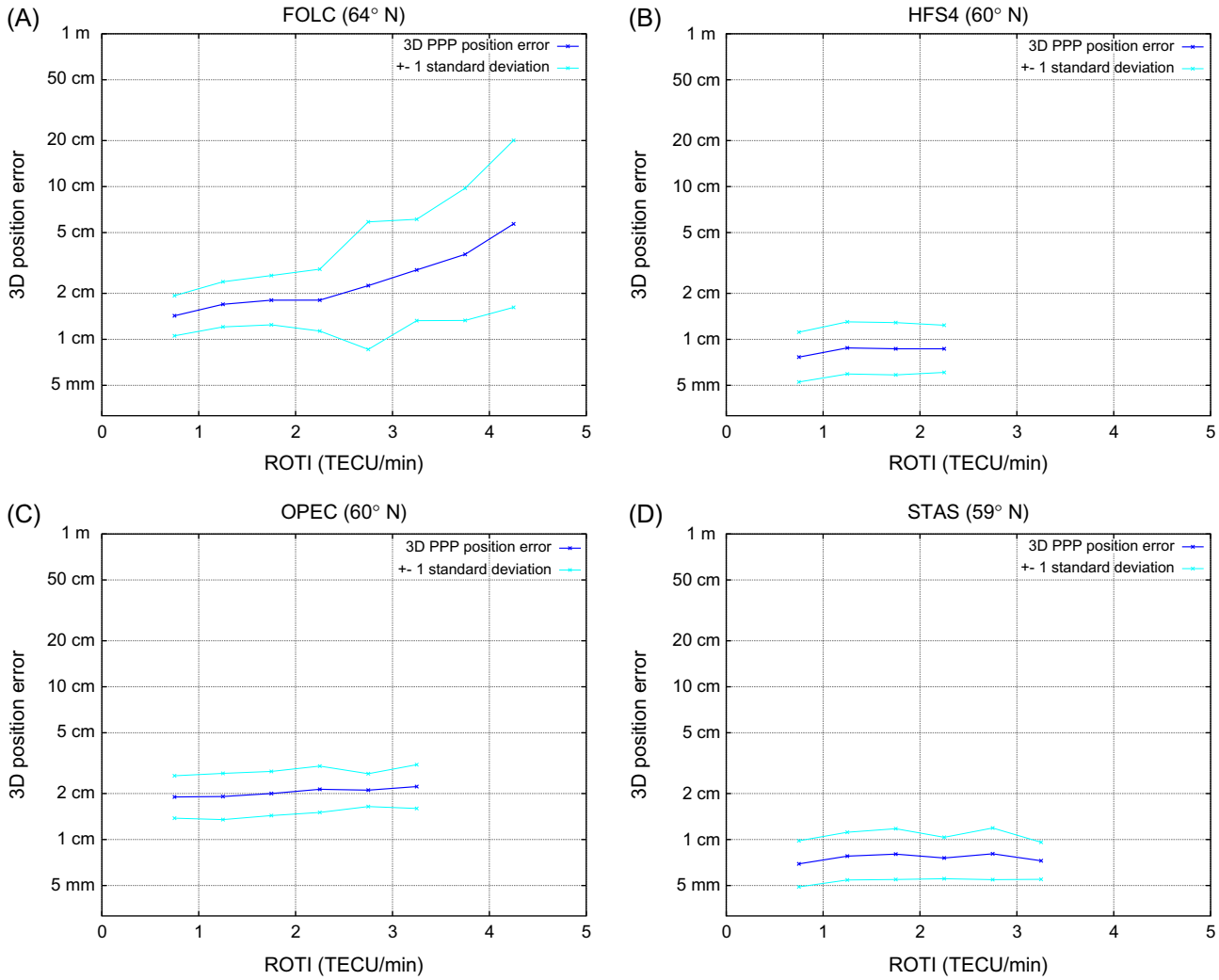

Fig. 4. Statistical relationship between mean ROTI and 3D position error, for these receivers: (A) FOLC, (B) HFS4, (C) OPEC, (D) STAS.

combination of inclined satellite orbits, the use of an elevation cutoff, and the general lack of receivers around the North Pole.

Figure 8 shows the mean ROTI for all the data from 2012, Figure 9 shows the percentage of observations which had a ROTI greater than or equal to 3.5 TECU/min, and Figure 10 shows the percentage of observations which had a ROTI greater than or equal to 5 TECU/min.

3.4. ROTI risk

Figures 11 and 12 contain tables showing the probability to have certain levels of ROTI simultaneously affecting several satellites observed by the same receiver. For each entry (colored square) in the figures, the probability was calculated simply as the percentage of ROTI measurement epochs (5 min resolution) in which the ROTI values simultaneously exceeded the defined level for the given number of satellites. The data set covers the entire year of 2012. As an example of how to read the tables, in Figure 12, panel B, the probability of simultaneously having two satellites at a ROTI value of at least 3 TECU/min is around 2%.

4. Discussion

The statistical analysis in Section 3.1 shows the connection between ROTI and PPP positioning errors. Table 3 lists the results of correlating ROTI values to 3D position errors. While the three receivers at the lowest latitudes (59°–60° North) show little to no correlation, the receivers at higher latitudes (64°–79° North) show a strong positive correlation. The best correlation is exhibited by the receivers TRO1 and HAMC, located at about 70° North. The missing correlation at low latitude receivers can be explained by the lack of strong ionospheric activity in those regions. Only strong events move the auroral oval far enough south to affect these receivers.

We note that the receivers with good correlations (above 64° North) have approximately the same value for the fit parameter b, indicating that the effect on the position error caused by increasing ROTI is roughly the same across this range of latitudes. The value of b varies slightly around 0.9 for these receivers, yielding the simple relation that the 3D position error is approximately exponentially proportional to ROTI. For the receiver NYAL, however, b is 1.67, which means an even stronger increase in position error as a function of ROTI. It is not clear why this is so, but we note that NYAL is the only site with a NetRS receiver (see Table 1), which is the oldest type of receiver among those used in this study. The receiver NYA1, which is colocated with NYAL, has an entirely different result that is more in line with the other receivers. It is plausible that the processing in the NetRS receiver is more vulnerable to noisy measurements than the newer generations of receivers.

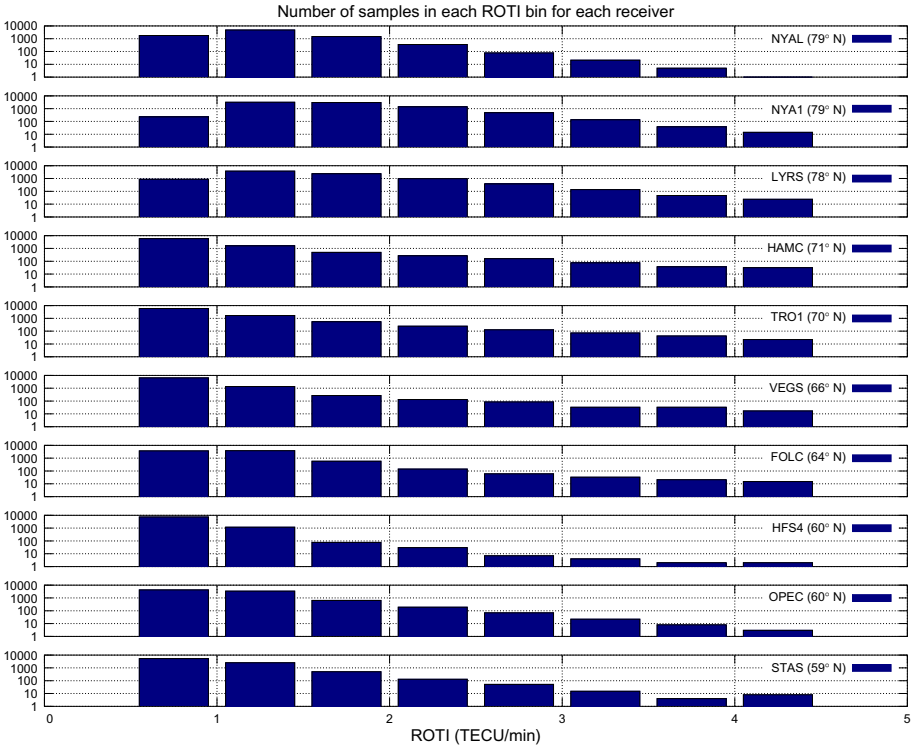

Fig. 5. Number of samples in the bins for Figures 3 and 4.

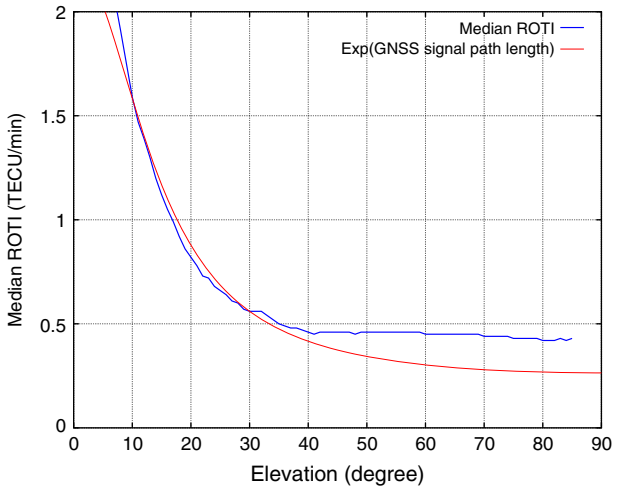

Fig. 6. Dependence of median ROTI (blue line) and the exponential of the GNSS signal path length (red line) on elevation. The red line is scaled to the ROTI level at 30° elevation.

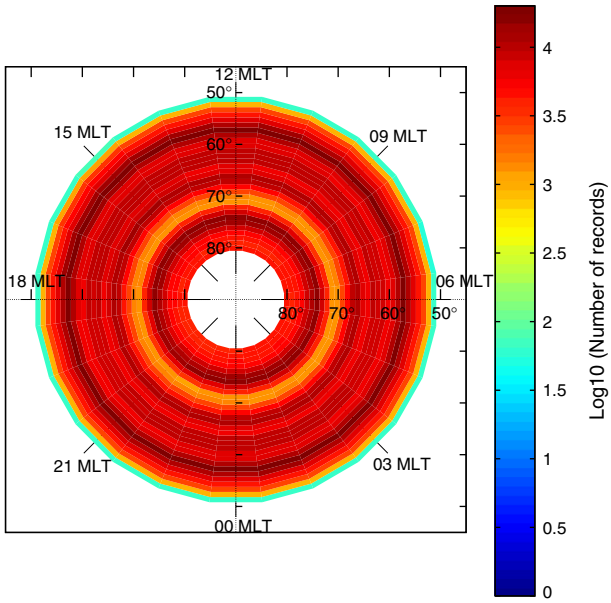

Fig. 7. Number of ROTI samples in each MLAT-MLT bin, with an elevation cutoff of 30°.

To make a classification of vulnerability by the type of receiver would require data from far more receivers than the number presented in this study. However, we expect that the relation between position error and ROTI will be exponential also for other types of receivers, although the proportionality may be somewhat weaker or stronger.

In Section 3.2 the effect of low elevations on ROTI values was presented. The elevation dependency of ROTI was significant at elevations up to 20°, very small at 30°, and negligible at 40°. Due to the inclination of the GNSS satellite orbits, satellites for receivers at high latitudes spend more time at low elevations, and never reach 90° elevation. This issue is more significant the farther north the receiver is located. Thus, it is generally preferred to set elevation cutoffs as low as possible. Based on the data shown in Figure 6, we chose to use an elevation cutoff of 30° for the ROTI statistics presented in Section 3.3 to avoid the issue of elevation dependency.

In Section 3.3 results regarding the location of elevated ROTI values in a geomagnetic reference frame (MLAT & MLT) were presented. The mean ROTI (Fig. 8) is elevated above 70° North on the dayside, and above 60° North on the nightside. Two regions have especially elevated values; the post-noon sector (12–16 MLT) at around 75°–80° North on

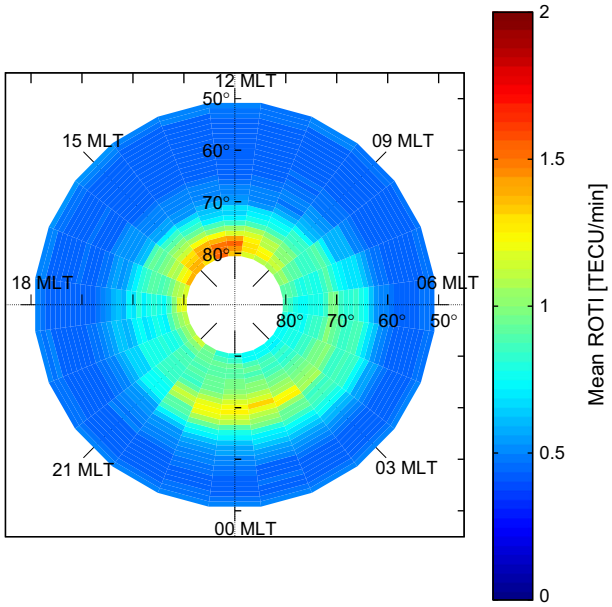

Fig. 8. Mean ROTI for 2012, with an elevation cutoff of 30°.

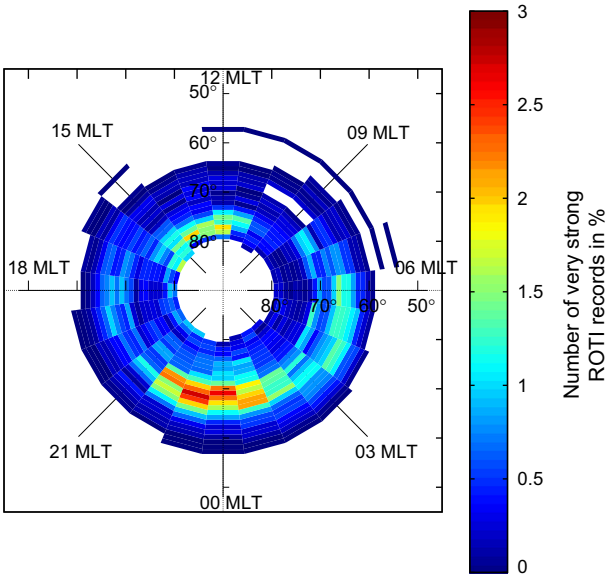

Fig. 10. Number of ROTI ≥5 TECU/min in percent, with an elevation cutoff of 30°. Note that the color scale is different from the color scale in Figure 9.

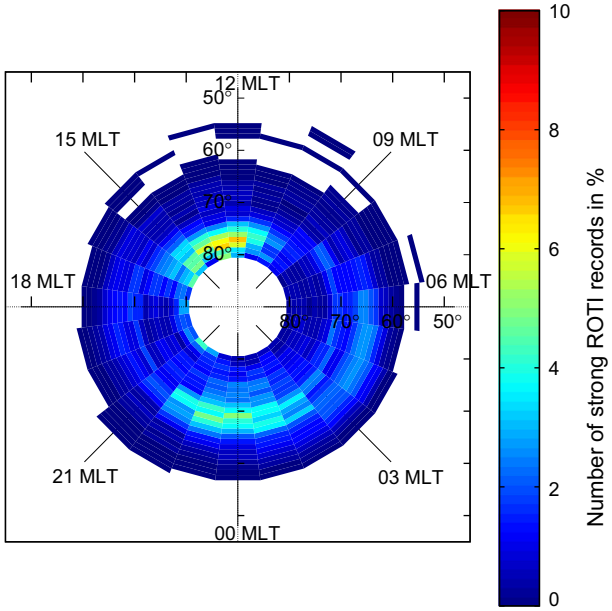

Fig. 9. Number of ROTI ≥3.5 TECU/min in percent, with an elevation cutoff of 30°.

the dayside, and the region around midnight (22–02 MLT) at around 70° North on the nightside. These regions correspond to the cusp region and the nightside auroral oval. The asymmetry observed for the ROTI distribution in the cusp region could be caused by an asymmetry in the values of the interplanetary magnetic field Y-component for the geomagnetic storms that occurred during 2012.

These regions are also found in the plots of occurrence of strong (≥3.5 TECU/min) and very strong (≥5 TECU/min) ROTI (Figs. 9 and 10). It is interesting to note that in the plot of strong ROTI, the occurrence is greater in the cusp region than at the nightside, but in the plot of very strong ROTI, the occurrence is much stronger in the nightside auroral oval region. This means that elevated ROTI values are more common in the cusp region, but when they occur in the nightside auroral oval region they are stronger than in the cusp.

In Section 3.4 tables showing the risk of simultaneously having several satellites with high ROTI values were presented. Generally, both the magnitude of ROTI, and the number of satellites affected, were higher for receivers at higher latitudes. For the northernmost receivers (Fig. 11, panels A–C), which are located at Svalbard, the maximum number of simultaneously affected satellites at high ROTI levels was somewhat less than that for receivers in the middle of Norway. This is caused by less satellites being visible at such a high latitude. Whether these risks are significant or not, depends on the kind of system that uses the data, and what thresholds are set for that system.

We note that Aquino et al. (2005) have made similar risk statistics for phase scintillation observed at Hammerfest, based on data from 2002 to 2003. The general pattern is the same as we see for ROTI at the same location (see Fig. 11, panel D), but with far lower probabilities.

5. Conclusions

- For receivers that experienced strong space weather effects (located above 64° North), there is a strong positive correlation between PPP error and ROTI. The 3D position error increases exponentially with increasing ROTI.
- For satellites at elevations below 30°, the increased signal path length through the ionosphere has a significant impact on ROTI values. For studies that investigate the condition of the ionosphere, ROTI values from low elevation satellites should be scaled to account for the elevation dependency of ROTI. Alternatively, one may avoid the issue by excluding data from satellites below 30° elevation. If one is instead studying the effects of ROTI on the receiver itself, the values should not be scaled or excluded, as the ROTI value is indeed a measure of the disturbance that the receiver observes in the GNSS observables. This should be taken into account when studying space weather with the use of ROTI.

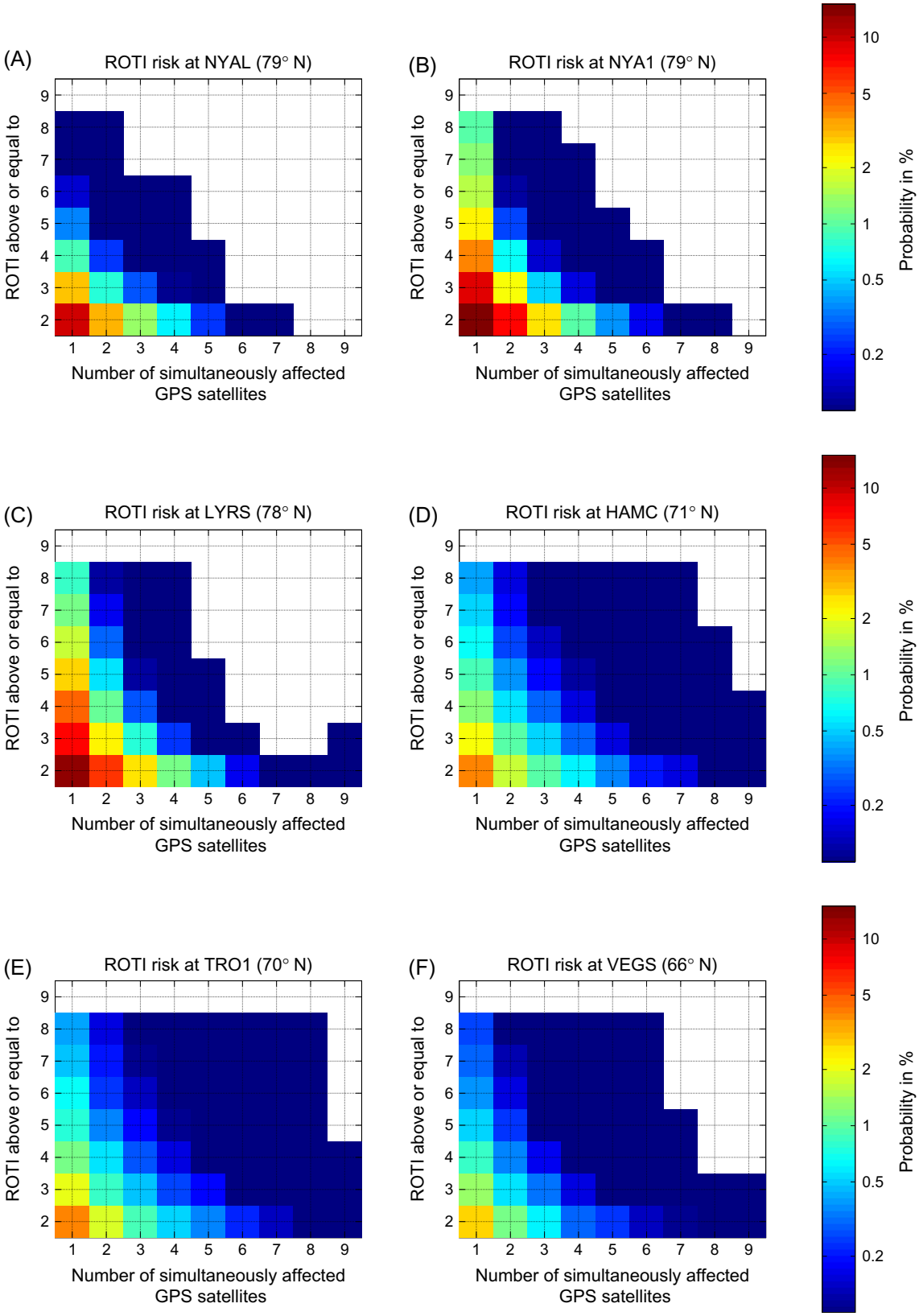

Fig. 11. Tables of the probabilities that ROTI exceeds threshold values simultaneously at several satellites, for these receivers: (A) NYAL, (B) NYA1, (C) LYRS, (D) HAMC, (E) TRO1, (F) VEGS.

– Elevated ROTI values occur mainly in the cusp region and in the nightside auroral oval. It most commonly occurs in the cusp region, but when it occurs in the nightside auroral oval, it is stronger.

– The risk of having several satellites observing enhanced ROTI values simultaneously is greater at higher latitudes. We have presented tables of the risks for receivers at different latitudes in Norway (Figs. 11 and 12).

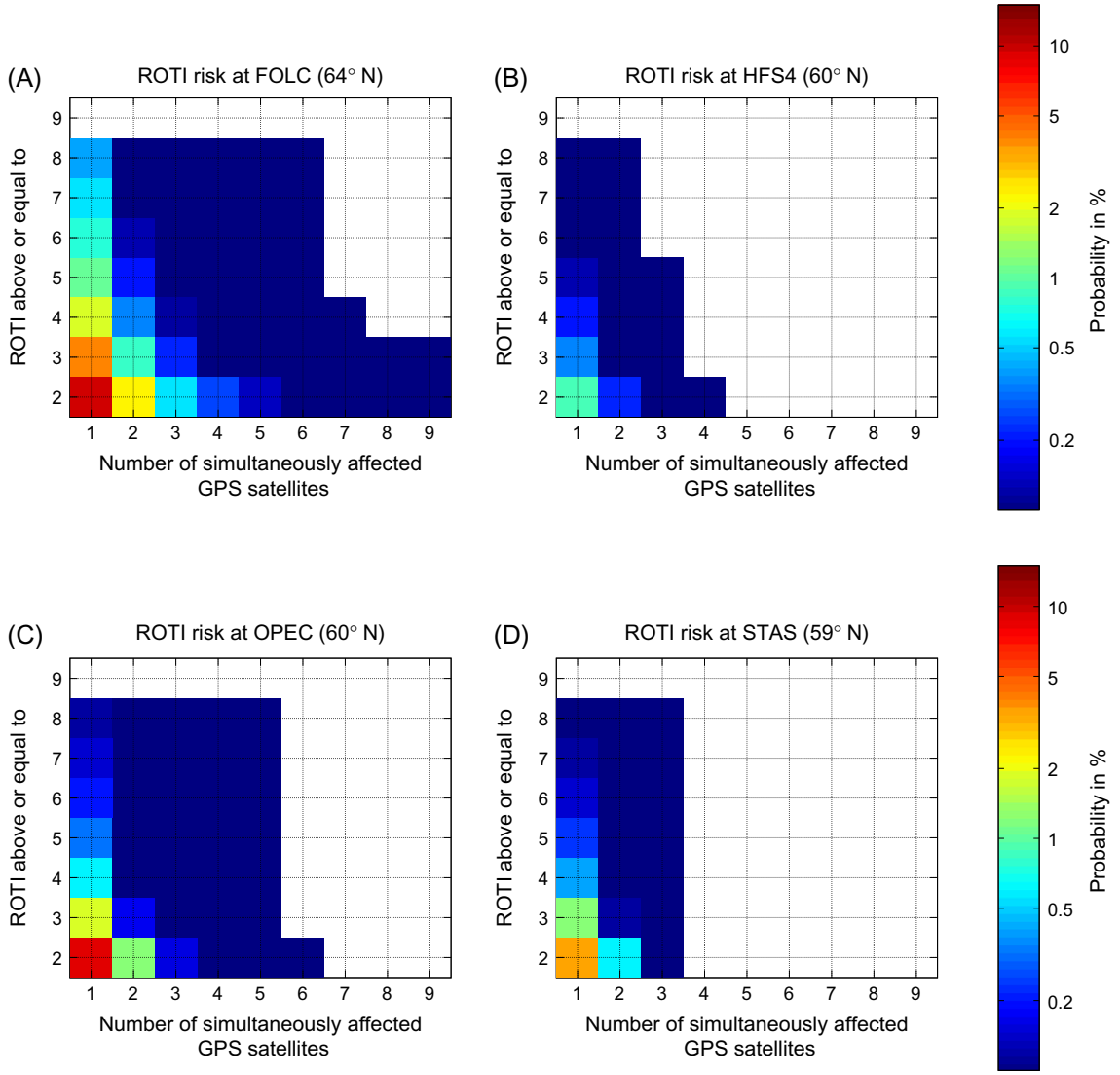

Fig. 12. Tables of the probabilities that ROTI exceeds threshold values simultaneously at several satellites, for these receivers: (A) FOLC, (B) HFS4, (C) OPEC, (D) STAS.

Acknowledgements. MLAT and MLT were computed using the Altitude Adjusted Corrected Geomagnetic Coordinate (AACGM) software. PPP solutions were computed using the GIPSY software, developed by NASA/JPL. The authors thank the reviewers for their helpful comments. The editor thanks two anonymous referees for their assistance in evaluating this paper.

References

Aarons, J., Global positioning system phase fluctuations at auroral latitudes, *J. Geophys. Res. [Space Phys.]*, **102 (A8)**, 17219–17231, DOI: 10.1029/97JA01118, 1997.

Aquino, M., F.S. Rodrigues, J. Souter, T. Moore, A. Dodson, and S. Waugh, Ionospheric scintillation and impact on GNSS users in Northern Europe: results of a 3 year study, *Space Communications*, **20 (1–2)**, 17–29, URL http://dl.acm.org/citation.cfm?id=1498858.1498862, 2005.

Basu, S., K. Groves, J. Quinn, and P. Doherty, A comparison of TEC fluctuations and scintillations at Ascension Island, *J. Atmos. Sol. Terr. Phys.*, **61 (16)**, 1219–1226, DOI: 10.1016/S1364-6826(99)00052-8, 1999.

Bertiger, W., S.D. Desai, B. Haines, N. Harvey, A.W. Moore, S. Owen, and J.P. Weiss, Single receiver phase ambiguity resolution with GPS data, *J. Geod.*, **84 (5)**, 327–337, DOI: 10.1007/s00190-010-0371-9, 2010.

Burston, R., I. Astin, C. Mitchell, L. Alfonsi, T. Pedersen, and S. Skone, Turbulent times in the northern polar ionosphere? *J. Geophys. Res. [Space Phys.]*, **115 (A4)**, A04310, DOI: 10.1029/2009JA014813, 2010.

Kersley, L., C.D. Russell, and D.L. Rice, Phase scintillation and irregularities in the northern polar ionosphere, *Radio Science*, **30 (3)**, 619–629, DOI: 10.1029/94RS03175, 1995.

Kivanc, Ö., and R.A. Heelis, Structures in ionospheric number density and velocity associated with polar cap ionization patches, *J. Geophys. Res. [Space Phys.]*, **102 (A1)**, 307–318, DOI: 10.1029/96JA03141, 1997.

Kouba, J., and P. Héroux, Precise point positioning using IGS orbit and clock products, *GPS Solutions*, **5 (2)**, 12–28, DOI: 10.1007/PL00012883, 2001.

Krankowski, A., I. Shagimuratov, L. Baran, I. Ephishov, and N. Tepenitzyna, The occurrence of polar cap patches in TEC fluctuations detected using GPS measurements in southern hemisphere, *Adv. Space Res.*, **38 (11)**, 2601–2609, Middle and Upper Atmospheres, Active Experiments, and Dusty Plasmas, DOI: 10.1016/j.asr.2005.12.006, 2006.

Moen, J., K. Oksavik, L. Alfonsi, Y. Daabakk, V. Romano, and L. Spogli, Space weather challenges of the polar cap ionosphere,

Journal of Space Weather and Space Climate, **3**, **A02**, DOI: 10.1051/swsc/2013025, 2013.

Moreno, B., S. Radicella, M.C. Lacy, M. Herraiz, and G. Rodriguez-Caderot, On the effects of the ionospheric disturbances on precise point positioning at equatorial latitudes, *GPS Solutions*, **15 (4)**, 381–390, DOI: 10.1007/s10291-010-0197-1, 2011.

Pi, X., A.J. Mannucci, U.J. Lindqwister, and C.M. Ho, Monitoring of global ionospheric irregularities using the worldwide GPS network, *Geophys. Res. Lett.*, **24 (18)**, 2283–2286, DOI: 10.1029/97GL02273, 1997.

Prikryl, P., R. Ghoddousi-Fard, B.S.R. Kunduri, E.G. Thomas, A.J. Coster, P.T. Jayachandran, E. Spanswick, and D.W. Danskin, GPS phase scintillation and proxy index at high latitudes during a moderate geomagnetic storm, *Ann. Geophys.*, **31 (5)**, 805–816, DOI: 10.5194/angeo-31-805-2013, 2013.

Prikryl, P., P.T. Jayachandran, S.C. Mushini, D. Pokhotelov, J.W. MacDougall, E. Donovan, E. Spanswick, and J.P. St. Maurice, GPS TEC, scintillation and cycle slips observed at high latitudes during solar minimum, *Ann. Geophys.*, **28 (6)**, 1307–1316, DOI: 10.5194/angeo-28-1307-2010, 2010.

Skone, S., M. Feng, R. Tiwari, and A. Coster, Characterizing ionospheric irregularities for auroral scintillations, in: Proceedings of the 22nd International Technical Meeting of the Satellite Division of the Institute of Navigation (ION GNSS 2009), Savannah, GA, 2009, pp. 2551–2558.

Spogli, L., L. Alfonsi, G. De Franceschi, V. Romano, M.H.O. Aquino, and A. Dodson, Climatology of GPS ionospheric scintillations over high and mid-latitude European regions, *Ann. Geophys.*, **27 (9)**, 3429–3437, DOI: 10.5194/angeo-27-3429-2009, 2009.

Tiwari, R., S. Bhattacharya, P.K. Purohit, and A.K. Gwal, Effect of TEC variation on GPS precise point at low latitude, *The Open Atmospheric Science Journal*, **3**, 1–12, DOI: 10.2174/1874282300903010001, 2009.

Tiwari, R., F. Ghafoori, O. Al-Fanek, O. Haddad, and S. Skone, Investigation of high latitude ionospheric scintillations observed in the Canadian region, in Proceedings of the 23rd International Technical Meeting of the Satellite Division of the Institute of Navigation (ION GNSS 2010), Portland, OR, 2010, pp. 349–360.

Weber, E.J., J.A. Klobuchar, J. Buchau, H.C. Carlson, R.C. Livingston, O. de la Beaujardiere, M. McCready, J.G. Moore, and G.J. Bishop, Polar cap F layer patches: structure and dynamics, *J. Geophys. Res. [Space Phys.]*, **91 (A11)**, 12121–12129, DOI: 10.1029/JA091iA11p12121, 1986.

Zumberge, J.F., M.B. Heflin, D.C. Jefferson, M.M. Watkins, and F.H. Webb, Precise point positioning for the efficient and robust analysis of GPS data from large networks, *J. Geophys. Res. [Solid Earth]*, **102 (B3)**, 5005–5017, DOI: 10.1029/96JB03860, 1997.

Cite this article as: Jacobsen KS & Dähnn M: Statistics of ionospheric disturbances and their correlation with GNSS positioning errors at high latitudes. J. Space Weather Space Clim., 2014, **4**, A27.